Cardiovascular Magnetic Resonance: Deeper Insights through Bioengineering.

AA Young[1] and JL Prince[2]

1. Department of Anatomy with Radiology, School of Medical Science, Faculty of Medical and Health Sciences, 85 Park Rd, Auckland 1023, New Zealand. a.young@auckland.ac.nz

2. William B. Kouwenhoven Professor of Electrical and Computer Engineering, Center for Imaging Science, John Hopkins University, 201B Clark Hall, 3400 North Charles Street, Baltimore, MD 21218. prince@jhu.edu

Abstract

Heart disease is the main cause of morbidity and mortality worldwide, with coronary artery disease, diabetes and obesity being major contributing factors. Cardiovascular magnetic resonance (CMR) can provide a wealth of quantitative information on the performance of the heart, without risk to the patient. Quantitative analyses of these data can substantially augment the diagnostic quality of CMR examinations, and can lead to more effective characterization of disease and quantification of treatment benefit. This review provides an overview of the current state of the art in CMR with particular regard to the quantification of motion, both microscopic and macroscopic, and the application of bioengineering analysis for the evaluation of cardiac mechanics. We discuss the current clinical practice and the likely advances in the next 5-10 years, and the ways in which clinical examinations can be augmented by bioengineering analysis of strain, compliance, and stress.

Introduction

Cardiovascular disease is the number one killer around the world, and its prevalence is growing due to the current epidemic of obesity and diabetes [1]. Although improvements in treatment have led to reductions in mortality, morbidity rates remain high, with substantial costs to society [1]. There is still a limited understanding of the pathological mechanisms underlying the various forms of heart failure and cardiac remodeling (changes in shape and function due to a worsening disease process). In particular there is a controversy about whether different presentations of heart failure represent distinct diseases or just opposite ends of a phenotypic spectrum [2,3]. Heart failure has traditionally been linked with reduced systolic function (as measured by the ejection fraction or proportion of blood ejected by the left ventricle) [4]. However, many patients present with normal ejection fraction and impaired filling characteristics [5]. Since clinical trials have failed to show benefit in patients with preserved ejection fraction using therapies that are recommended for those with reduced ejection fraction, it is apparent that the pathophysiological differences between the two syndromes require different treatment approaches [6]. Because of this, complete characterization of a patient's clinical status is critical for successful treatment.

Cardiovascular magnetic resonance (CMR) imaging provides a wealth of detailed, high quality, quantitative information on heart structure and function. Advantages of CMR include its lack of ionizing radiation, its ability to image the entire heart regardless of the orientation and shape of the heart and the presence of surrounding structures, and its ability to produce different contrasts according to different physiological mechanisms. CMR imaging can provide detailed information on 3D ventricular shape and geometry [7] [8], regional systolic [9] and diastolic [10] strain, material microstructure [11] [12] , blood flow [13], perfusion [14] and viability [15] [16]. It is considered the most accurate method to measure ventricular volumes and systolic function [17]. It is also considered to be the best method for

the evaluation of congenital heart disease [18]. The high precision and accuracy of CMR [19] has led to its increasing application worldwide in cardiac research studies and clinical practice [20,21].

CMR can provide a range of valuable data for the analysis of cardiac function using bioengineering methods. The sensitivity of CMR to motion, both macroscopic and microscopic, gives insight into the mechanical function, haemodynamics, microstructure, and tissue properties. Biophysical analysis adds value to the clinical utility of the images by enabling characterization of the underlying pathophysiological processes. Dimension reduction techniques and statistical characterization of patient groups enables quantitative analysis of shape change and regional wall motion abnormalities. This review gives an overview of the ways in which CMR can quantify structure and function, with emphasis on how CMR can be used to solve bioengineering problems in the heart, and how bioengineering methods can be used to interpret the data in terms of the physiological processes underlying disease.

Basic Principles

Briefly, certain atomic nuclei (e.g., ^{1}H, ^{23}Na, ^{19}F) possess the quantum property of spin, which yields an endogenous magnetic moment. Hydrogen (proton) imaging is used in most clinical applications due to its high abundance and relatively strong magnetic moment. When placed in a strong external magnetic field, typically 1.5-9.4 Tesla, a net magnetization is obtained aligned with the direction of the main magnetic field, typically in the head-foot or longitudinal direction. An excitation of the hydrogen nuclei is achieved using a radiofrequency (RF) pulse tuned to the resonant frequency of the nuclei. The resonant frequency is given by the Larmor equation:

$$\omega = \gamma B \qquad (1)$$

where γ is the gyromagnetic ratio (42.58 MHz/Tesla for hydrogen) and B is the strength of the magnetic field. The RF pulse causes a tilt (or “flip”) of the magnetization toward the orthogonal (transverse) plane

and the spins then precess in synchrony at the resonant frequency, giving rise to an oscillating magnetic field which can be detected in a local coil placed adjacent to the tissue of interest. The signal is detected in quadrature, giving both magnitude and phase. Over time the spins relax back to their ground state through two main mechanisms, giving rise to two exponential relaxation constants T_1 and T_2. T_1 or longitudinal relaxation is due to energy being lost to the molecular environment and measures the growth of the longitudinal magnetization back to the baseline value. T_2 or transverse relaxation is due to dephasing of nuclei due to inhomogeneities in the local magnetic field and local electromagnetic effects, and measures the decay of the transverse magnetization. For normal myocardium, T_1 is about 800 msec and T_2 is about 30 msec.

Figure 1 shows a basic excitation and detection pulse sequence (gradient recalled echo). Adjustment of the repetition time (T_R) and echo time (T_E) and spin preparation pulses can give the image a T_1, T_2, or proton density weighting. Although maximum signal is achieved using a flip angle (α) equal to 90-degrees, smaller flip angles are usually used in order to acquire images faster in a so-called steady-state mode.

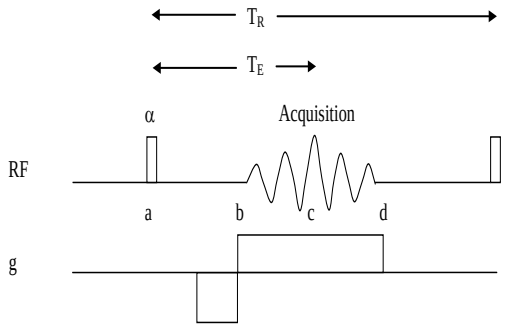

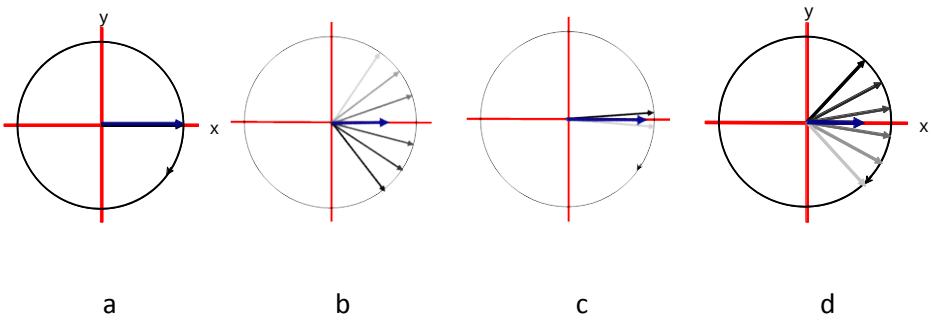

Figure 1. A gradient recalled echo pulse sequence. An initial RF pulse flips the magnetization into the transverse plane (a). In the presence of a gradient, dephasing occurs due position (b). A refocusing gradient reverses the relative phase, and an echo is formed as the spins rephase at T_E (c). Phase accrual continues until the end of the gradient (d).

Imaging is performed by applying transient magnetic fields in the form of a gradient in the B_z component of the magnetic field, which thereby encodes position in the relative phase of the transverse magnetization. The addition of a gradient in the magnetic field acts to change the frequency of precession, so that the accumulated phase is given by

$$\theta(\boldsymbol{x},t) = \gamma \int_0^t \boldsymbol{g}(\tau)\cdot\boldsymbol{x}(\tau)d\tau = \boldsymbol{x}\cdot\boldsymbol{k} \qquad (2)$$

assuming constant **x**, where **k** is a wavevector with units of m^{-1}, dependent on the gradient waveform:

$$k = \gamma \int_0^t \boldsymbol{g}(\tau)d\tau \qquad (3)$$

The signal is given by the integral of spins across the domain, giving a Fourier relationship between the image domain and the acquisition domain (known as k-space):

$$S(\boldsymbol{k}) = \int M_{\perp}(\boldsymbol{x}) \exp(-j\boldsymbol{k} \cdot \boldsymbol{x}) d\boldsymbol{x} \quad (4)$$

Contrast can be made dependent on proton density or the T_1 or T_2 relaxation time constants by applying different pulse sequences (timing and magnitude of RF pulses and gradients). Contrast can also be made to be dependent on velocity, displacement, or diffusion as discussed below.

Disadvantages of CMR include the relatively slow image acquisition relative to computed tomography or ultrasound. Since typically only one line of k-space is acquired per excitation, many excitations are required to build up a 2D or 3D image using different gradient magnitudes and directions, which is then transformed into the image domain using a fast Fourier transform. Also the presence of a strong magnetic field makes it unsafe to image patients with implanted defibrillators or pacemakers. A considerable infrastructure is required since the scanner room must be shielded from external RF energy using a Faraday cage built into the walls floors and ceiling.

Morphometry

The standard CMR clinical assessment of global volume, mass, and regional wall motion abnormalities is multiple 2D breath-hold cine steady state free precession (SSFP) imaging (also known as true-FISP, FIESTA, and BFFE by the various scanner manufacturers) [22,23]. In this technique, the magnetization is brought into a coherent steady state with very short T_R and balanced gradients (all gradient waveforms are symmetric). Image contrast is dependent on the ratio of T_1 to T_2, which gives excellent demarcation between muscle, blood, fat, and air (Figure 2).

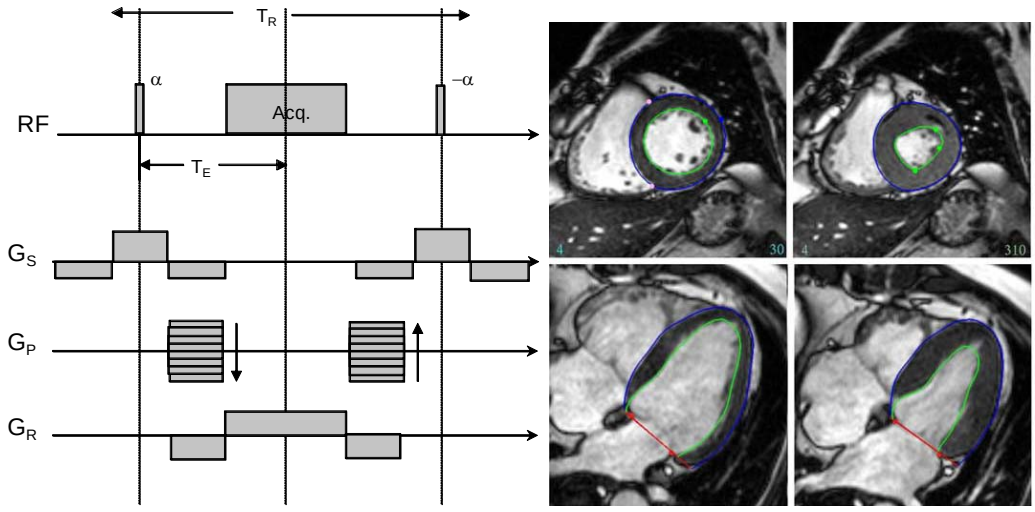

a b

Figure 2. SSFP pulse sequence and resulting images. a) all gradients are balanced giving rise to a coherent steady state with high signal and short TR. b) high contrast is achieved dependent on the ratio of T1:T2. c) Embedded video showing 3D reconstruction of left ventricle through the cardiac cycle; the model is not critically dependent on the exact location of the images.

A high signal to noise ratio is achieved due to the coherent steady state, with a magnitude proportional to the ratio of T_1 to T_2:

$$S = \frac{M_0 T_2}{T_1 + T_2}(e^{-T_E/T_2}) \qquad (5)$$

Typical scan parameters include contiguous short axis slices 5-10 mm thick, field of view 300-400 mm, TR = 3 msec, T_E = 1.6 msec, flip angle = 60 degrees, image matrix = 256x200, 25-50 cine frames per slice, breath-hold duration = 8-15 sec.

SSFP images are typically analyzed for scientific or clinical use by manual or semi-automatic contouring of the inner and outer boundaries of the heart (epicardial and endocardial) after which the outlined areas are converted to volumes and summed to produce estimates of volume and mass [7]. This produces accurate and reproducible quantification of left and right ventricle mass and volume [8,24,25]. Fully automatic segmentation techniques are becoming available [26], and these promise to provide robust automated analysis in the near future. The major source of error in the calculation of mass and volume is the demarcation of the base near the mitral and aortic valves, due to the difficulty of separating ventricular from atrial myocardium and the large motion of the base through the plane of the short axis image (typically 10-15mm) [27,28]. Short axis images also give rise to significant partial voluming (mixture of different tissues within a voxel) at the apex due to curvature through the thick slice. Inclusion of long axis slices (typically two chamber, four chamber, and three chamber views as shown in Figure 2) enable better delineation of the apex and base. A 3D mathematical modeling approach enables accurate quantification of all structures with minimal user interaction [29]. Information from short and long axis slices, as well as temporal coherence, can be integrated in real time to achieve interactive assessment of pump function [30]. Non-rigid registration methods can be incorporated to track the boundaries through the cardiac cycle, giving greater reproducibility [31].

Regional function can be quantified by dividing the heart in to standard segments which can be analysed for wall thickening and local volume change [32]. Asynchrony measures, which quantify the variation in time that it takes different segments to reach peak ejection, have been shown to predict mortality after cardiac resynchronization therapy [33].

Perfusion, Fibrosis, and Hypertrophy

Gadolinium (Gd) contrast agents, which reduce the T_1 of adjacent tissue, can be used to quantify local perfusion, extracellular volume, and water exchange rates among vascular, interstitial, and cellular

spaces [34]. Perfusion can be quantified by analyzing the kinetics of the first pass of a Gd bolus through the myocardium [35], [36]. T1 fast imaging methods are used to obtain images at ~1 sec temporal resolution for ~30-60 seconds. Blood flow can then be quantified in units of ml/min per gram of tissue using either model-based or model-independent methods. Model-based approaches specify the functional spaces in myocardial tissue and the kinetics between these spaces (mainly the vascular and extracellular spaces since intracellular space is excluded from most Gd chelates) [37]. These methods have the advantage of providing estimates for the vascular volume and capillary permeability surface area product, but the model parameters are clinically difficult to identify [36]. Model-independent methods make use of the Fick principle (mass balance). The myocardial signal is given by a convolution of the arterial input function with a tissue response function. Normalized by the blood flow, the tissue response function gives the probability that a tracer particle entering at time t=0 remains in the region at subsequent time t. Axel [38] proposed that the form of the tissue response function is well modeled by a Fermi function, if the analysis window does not exceed the first pass. Pixel based analysis methods are possible using non-rigid registration and correction for coil sensitivity [39].

Endogenous perfusion contrast is also available by arterial spin labeling [40] or blood oxygen level dependence (BOLD) [41]. In the future, hyperpolarized media may be used as contrast agents [42].

Late gadolinium enhancement (LGE) infarct mapping is an important marker of infarction in regional disease [15] [43]. This technique relies on leakage of contrast from the vascular to the extracellular space, and subsequent wash-out of contrast. The kinetics of this wash-in/wash-out phenomenon are very different in normal and infarcted tissue, and is most apparent 10-30 min after injection when Gd contrast is washed-out of normal tissue but remains in the infarct. Imaging at this time yields LGE maps highlighting areas of scar or irreversibly damaged myocardium which will not recover function after revascularization [15]. The transmural extent of LGE is predictive of wall motion recovery after

revascularization and post-infarct adverse remodeling [15,44]. LGE can also detect fibrosis in hypertrophic cardiomyopathy (HCM) [45], hypertension [46], and diabetes [47]. The “grey zone” surrounding an infarct is associated with arrhythmia inducibility and mortality [48].

Myocardial fibrosis is also important in identifying diffuse disease leading to heart failure [49]. T1 mapping enables the quantification of absolute T_1 before and after the administration of contrast and thereby can measure the concentration of Gd in myocardium [50]. Recent advances in T_1 mapping enable fast robust quantification of T_1 maps in humans [48]. In patients with heart failure, post contrast T_1 has been shown to correlate with fibrosis and to be shorter in patients with more severe diastolic function [49]. Correlations between T_1 and fibrosis were also found in patients with aortic stenosis and HCM [51].

T_1 mapping pre and post Gd administration provides estimation of extracellular blood volume (ECV), assuming that $\%ECVm = (100\text{-}Hct)\Delta R_{1m}/\Delta R_{1b}$ where ΔR_{1m} is the change in relaxation rate ($1/T_1$) of myocardium pre to post contrast, ΔR_{1b} is the change in relaxation rate of blood, and Hct is the hematocrit [52]. ECV is increased in myocardial infarction (in the infarct and also in the remote zone), in patients with non-ischemic cardiomyopathy, and in older volunteers [53]. Care must be taken in interpreting the results since ECV is increased in fibrosis, but also with inflammation and edema [54].

It may also be possible to estimate myocyte cell size using T_1 mapping pre and post contrast [55], using a two-site water exchange model to estimate the intracellular lifetime of water, which is strongly correlated with cell volume and minor axis dimension. This method may provide noninvasive estimates of cellular hypertrophy. Figure 3 shows examples of perfusion and T1 mapping.

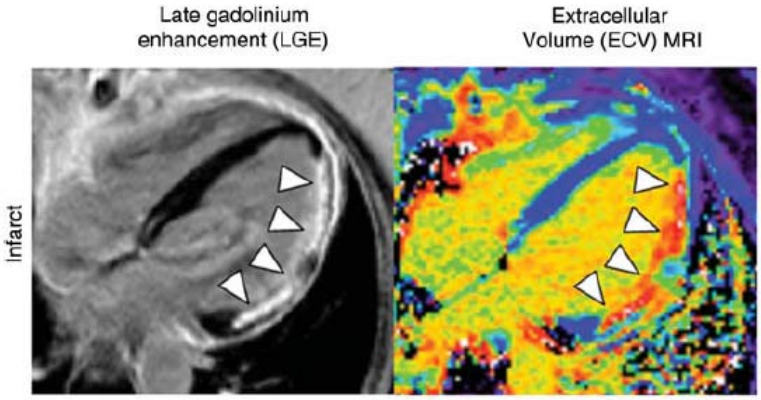

a b

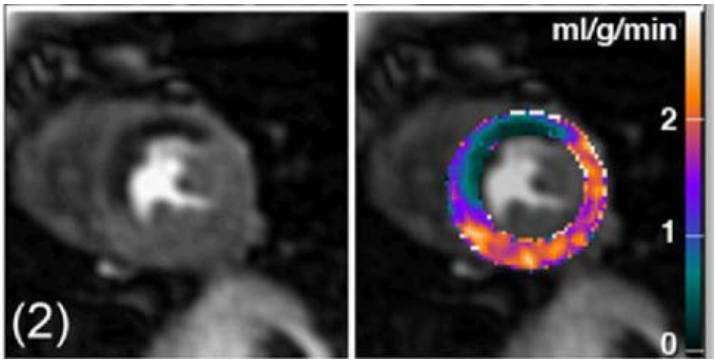

c d

Figure 3. Mapping tissue characteristics using magnetic resonance contrast agents. a) Late gadolinium enhancement shows areas of non-viable (scar) tissue (arrows). b) T1 mapping quantifies extracellular volume in % c) first pass contrast hypo-enhancement shows area of perfusion defect. d) Quantitative map of perfusion in ml/g/min obtained from first pass perfusion scan [39,53]. Embedded video shows time course of perfusion scan, showing uptake of contrast by the myocardium over a period of ~30 seconds, and the perfusion parameters derived, at rest and during adenosine stress.

Microstructure

MRI can also examine the microstructure of the heart using endogenous or exogenous contrast mechanisms. A useful endogenous contrast is given from diffusion weighted imaging. The basic pulse sequence is the same as Figure 1, with the addition of diffusion encoding gradients. Incoherent motion, due for example to the random diffusion of water, will result in signal loss due to dephasing [56] [57].

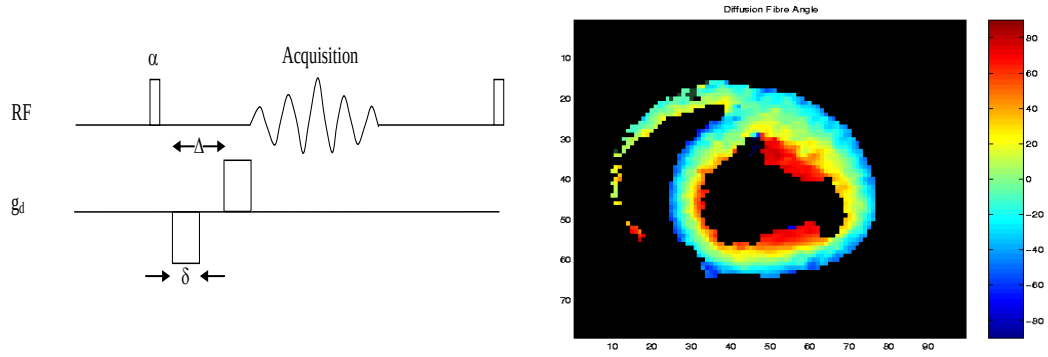

a b

Figure 4. Quantifying microstructure using diffusion weighted imaging. a) diffusion encoding using a bipolar gradient. b) direction of maximal diffusivity given from the orientation of the eigenvector associated with the maximum eigenvalue of the diffusion tensor. c) diffusion tensor tractography in a normal rat heart. d) fiber disarray due to myocardial infarction [58] [59].

The change in phase due to displacement **u** over the time interval Δ is given by:

$$\theta(u,t) = \gamma \int_0^{\Delta} \boldsymbol{g}_d(\tau) \cdot \boldsymbol{x}(\tau) d\tau = \boldsymbol{u} \cdot \boldsymbol{q} \qquad (6)$$

where **q** is given from the integral of the gradient waveform analogous to **k** in eqn. 3:

$$\boldsymbol{q} = \gamma \boldsymbol{g}_d \delta \,. \qquad (7)$$

The signal loss is given by

$$S(\boldsymbol{q},\Delta) = S(\boldsymbol{0},\Delta)\int P(\boldsymbol{u},\Delta)\exp(j\boldsymbol{q}\cdot\boldsymbol{u})d\boldsymbol{u} \quad (8)$$

where P is the average probability distribution function of particle displacement (called the ensemble average propagator). By acquiring diffusion weighted images at different encoding strengths, it is possible to obtain a spectrum of diffusivity in each voxel. There is a Fourier relationship between the diffusion domain and the acquisition domain (called q space). By applying the diffusion sensitive gradients in different orientations (at least 6 but typically more), the 3D diffusion propagator can be quantified. Assuming a Gaussian propagator, the apparent diffusion can be represented by a second order tensor in each voxel [57]. The eigenvectors associated with the maximum and minimum eigenvalues of this tensor give the directions of maximum and minimum diffusivity, which correspond to the direction of the muscle cells and layers respectively [11] [60]. If several families of fibers can be present in a single voxel, the propagator can be approximated by an orientation distribution function often represented by a combination of spherical harmonics [61]. Tracking of fibers in the heart leads to interesting patterns in healthy and diseased hearts [59]. However, interpretation of cardiac structure in terms of discrete muscle bundles can be problematic since microscopy data shows myocardium to be a continuously branching syncytium [62], rather than discrete bundles.

Recently there has been renewed interest in quantifying the fiber architecture in-vivo [63] [60] [64]. Promising results are being obtained using a stimulated echo version of the diffusion weighted sequence. Since any strain will also lead to a signal loss, the timing of the first gradient and second gradients is carefully controlled so that the mean strain between them is zero [65]. In fact, a very similar pulse sequence with different timing is used to measure displacement [66] and strain [67] in the heart (see Kinematics).

Diffusion tensor imaging has been used to investigate the changes in architecture due to pathology and disease. Hsu *et al.* [11] found a decrease of apparent diffusion within hours after the induction of myocardial infarction by occlusion of the left anterior descending coronary artery in rabbits. Chen *et al.* [68] found increased diffusion and decreased anisotropy in rats. Similar results have been observed in pigs [69]. The remodeling of fibers was dependent on the size of the infarct and its location (basal vs apical) [70], with a shift toward more left-handed fibers occurring in the group with apical septal infarcts. In contrast, Strijkers *et al.* [71] found increased anisotropy in mice after infarction. Using in-vivo DTI in humans, Wu *et al.* [64,72] found an increased diffusion and decreased anisotropy in the infarct zone with a change in the proportion of left to right handed fibers. In the progression to chronic infarction, diffusion decreased and anisotropy increased. Further work is needed to investigate the effect of infarct location on the remodeling of fiber architecture in humans.

Flow

MRI has the unique ability to quantify velocity at each pixel in any direction. The phase of the image is made sensitive to motion using motion encoding gradients (Figure 5). An initial gradient lobe wraps the spins along a particular axis, the second lobe rewinds the spins resulting in no change in phase if no motion occurs. For spins that coherently move an amount **u** during Δ, the phase shift is $\phi = \gamma\delta\mathbf{g}.\mathbf{u}$ (assuming an ideal gradient profile). If the time interval Δ is kept small there is little time for T2 decay and the displacement over Δ can used as an estimate of velocity. This method is essentially the same as the diffusion weighted sequence of Figure 4; however in flow imaging the phase is interrogated for coherent motion, compared with the magnitude in the case of incoherent motion.

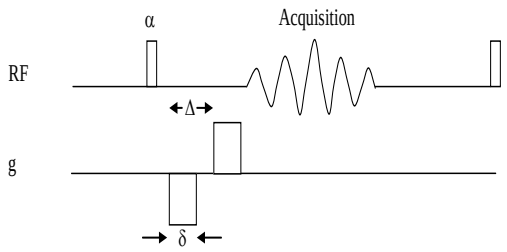

a

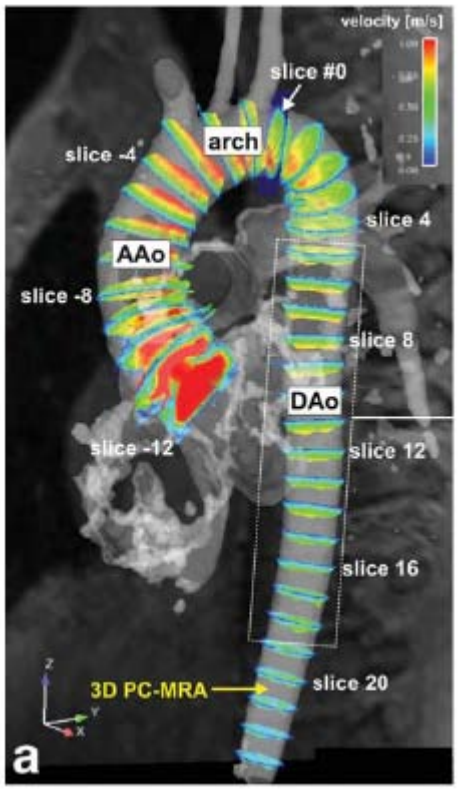

b

Figure 5 Velocity measurement using a bipolar gradient. a) velocity encoding using a bipolar gradient. b) three-dimensional time resolved flow showing velocity at different points in the aorta. These can be used to calculate pulse wave velocity, a measure of aortic compliance (a marker of vascular disease). Embedded video shows 4D flow animation [73].

In practice two scans must be acquired with different velocity encoding gradient strengths, to allow subtraction of phase offsets arising from sources other than motion. Separate acquisitions with velocity encoding gradients in the x, y, and z directions allow the calculation of all components of the velocity vector. Recently there has been considerable interest in 3D time resolved acquisition of the 3D velocity field in the heart and great vessels (known as 4D flow) [74]. This technique shows promise in the evaluation of haemodynamics in patients with flow anomalies. In congenital heart disease, an image based surgical planning framework can predict the effects of various interventions using patient specific computational fluid dynamics (CFD) simulations [75]. 4D flow patterns have been useful in the evaluation of patients after the Fontan procedure [76]) or those with a single ventricle [77].

By encoding velocity with several different gradient magnitudes, an image of the velocity spectrum can be obtained. The change in phase due to a constant velocity $\boldsymbol{v}$ is

$$\theta(\boldsymbol{v},t) = \gamma \int_0^t \boldsymbol{g}(\tau)\cdot\boldsymbol{x}(\tau)d\tau = \boldsymbol{v}\cdot\boldsymbol{k}_v \tag{9}$$

$$\boldsymbol{k}_v = \gamma \int_0^{\Delta} \boldsymbol{g}(\tau)\tau d\tau \tag{10}$$

In an analogous manner to the Fourier encoding of position, there is a Fourier relationship between the velocity domain and the acquisition domain:

$$S(\boldsymbol{q}) = \int P(\boldsymbol{v})\exp(-j\boldsymbol{k}_v\cdot\boldsymbol{v})d\boldsymbol{v} \tag{11}$$

where P($\boldsymbol{v}$) is a probability density distribution for velocity within each voxel.

In turbulent jets, incoherent motion leads to phase dispersal and signal loss in velocity encoded imaging [78]. This can lead to significant errors in the phase estimate of velocity, which can be ameliorated by

reducing the TE of the sequence [79]. On the other hand, the signal loss phenomenon can be exploited to quantify the severity of turbulent jets in patients with aortic stenosis [80]. In this method, several velocity encoded images are acquired at different encoding strengths. Assuming a Gaussian distribution for the velocity in each voxel, the signal loss with respect to two encoding strengths (leading to $\mathbf{k}_v$ values $\mathbf{k}_{v1}$ and $\mathbf{k}_{v2}$) can be quantified as follows: [81] [82]

$$\sigma^2(k_{v1}^2 - k_{v2}^2) = 2\ln\left(\frac{\left|S(k_{v2})\right|}{\left|S(k_{v1})\right|}\right) \tag{12}$$

This is similar to the method used to quantify diffusion (above) and turbulence spectral imaging can also be performed in a fashion similar to diffusion spectrum imaging.

Velocity imaging can be tuned to capture the motion and strain-rate of myocardium, where it is sometimes termed tissue phase mapping [83,84]. The Cartesian rate of deformation tensor *V* is derived from the spatial derivative of velocity:

$$V = \frac{1}{2}(D + D^T); \quad D = \frac{\partial \mathbf{v}}{\partial \mathbf{x}}; \tag{13}$$

A stimulated echo version of the velocity encoding sequence was used by Wedeen *et al.* [85] to encode velocity at multiple points in time but to image at only a single fixed time, thus creating "motionless movies" in which the velocity and strain rate show as time-changing image intensities on a reference image of anatomy that does not move.

Kinematics

Global performance and regional pump function are useful parameters of cardiac disease. However, they only provide indirect measures of the underlying myocardial function. CMR can also provide

quantitative myocardial displacement and velocity information in all directions and in all regions of the heart. Displacement and strain imaging can be performed routinely in the clinical setting using a variety of methods, as outlined below.

SPAMM: Selective saturation pulses can be used to alter the pattern of magnetization within the tissue, before an imaging sequence is played out. These have been used for many years to null the signal in specific regions of the image in order to label and track tissue and blood [86] [87]. In 1989 Axel and Dougherty [88] developed an efficient nonselective magnetization preparation pulse sequence called spatial modulation of magnetization (SPAMM), which in its most basic form produces a cosine modulation of the longitudinal magnetization (Figure 6). An initial 90° RF pulse is applied to rotate the longitudinal magnetization into the transverse plane. A gradient is then applied to encode position in the phase of the magnetization along the gradient direction. A second 90° pulse rotates the magnetization back to the longitudinal direction. After a period of time in which the transverse component has been removed due to T_2 relaxation or a crusher gradient, the longitudinal magnetization profile (ignoring T_1 relaxation) is cosine modulated.

$$M_z = M_0(\boldsymbol{X})\cos(\boldsymbol{k_e} \cdot \boldsymbol{X}) \tag{14}$$

A standard gradient echo imaging sequence is then applied to image the resulting tag pattern as it deforms throughout the cardiac cycle. With the addition of more RF pulses (commonly with amplitudes given from a binomial sequence) the tag pattern can be shaped into more of a square wave. Applying two such preparations in orthogonal directions gives a characteristic grid pattern. The effect of T_1 relaxation is to reduce the tag contrast over time and add an untagged component which grows over time.

$$M_z = M_0(1-\exp(-t/T_1)) + M_0\cos(\boldsymbol{k_e} \cdot \boldsymbol{X})\exp(-t/T_1) \tag{15}$$

By changing the phase of the second RF pulse it is possible to achieve a negative cosine modulation (Figure 6). Subtracting the two complementary acquisitions (known as complementary SPAMM or CSPAMM) removes the relaxed magnetization and improves tag contrast.

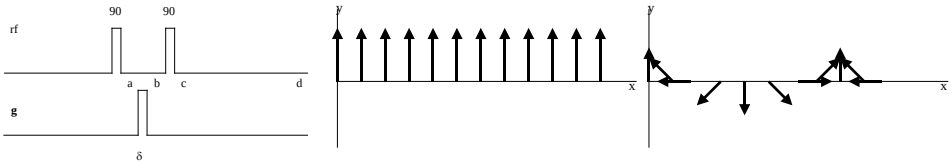

a b c

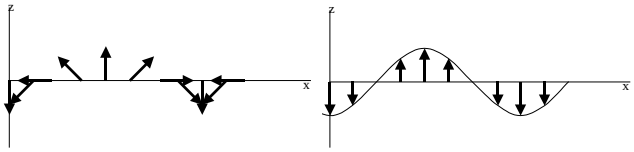

d e

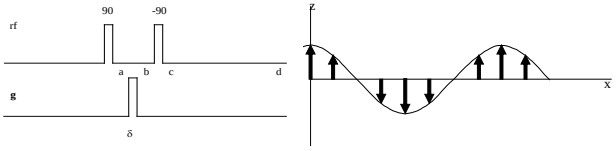

f g

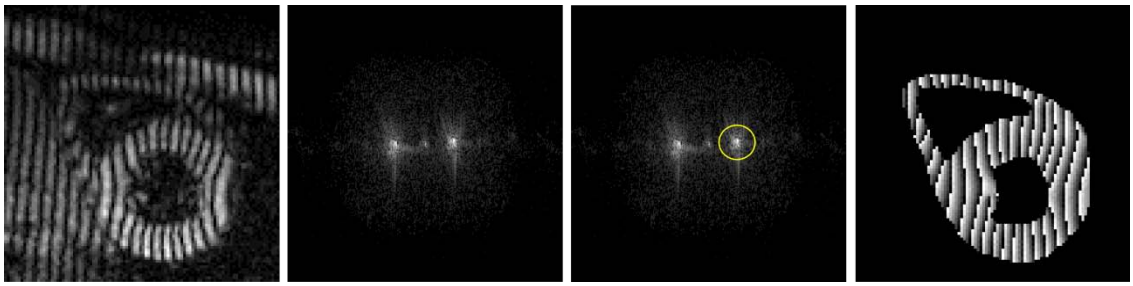

h i j k

Figure 6 SPAMM tagging. a) Pulse sequence known as 1-1 SPAMM tagging. b) Initial magnetization at after the first RF pulse (a). c) Phase wrapped in the x direction after the gradient. d) Wrapped magnetization stored in the longitudinal direction. e) Cosine modulation remains after crushing the transverse component (z is in the longitudinal direction, x and y in the transverse plane). f) CSPAMM sequence. g) Complementary modulation which can be used to subtract untagged contamination arising from T1 relaxation. h) SPAMM tagged image at end-systole. i) k space representations showing harmonic peaks. j) Hilbert filter isolating one peak. k) Image domain phase after inverse Fourier transform. This harmonic phase is constant through time for each material point. Embedded video shows computer strain in a patient with an infarct, movie courtesy of Donel Tani, Diagnosoft, Inc.

The analysis of the tag pattern has been performed using several image processing methods, including active contour models [89], model tags [90], Gabor filtering [91], optical flow [92] and non-rigid registration [93,94]. However these methods can be computationally intensive and often require user correction.

HARP: Osman *et al.* [95,96] developed a fast analysis for MR tagged images based on the harmonic phase (HARP) image. If **X**(**x**) denotes an Eulerian deformation map, giving the material point position **X** as a function of current position **x**, then ignoring T_1 effects the longitudinal magnetization at time t is

$$M_z(\boldsymbol{x}) = M_0(\boldsymbol{X}(\boldsymbol{x}))\cos(\boldsymbol{k_e}\cdot\boldsymbol{X}(\boldsymbol{x})) = \frac{M_0(\boldsymbol{X}(\boldsymbol{x}))}{2}\left(\exp(j\boldsymbol{k}_e\cdot\boldsymbol{X}(\boldsymbol{x})) + \exp(-j\boldsymbol{k}_e\cdot\boldsymbol{X}(\boldsymbol{x}))\right) \quad (16)$$

The location of the peaks in the Fourier domain are given from the Fourier shift theorem

$$g(\boldsymbol{X})\exp(j\boldsymbol{X}\cdot\boldsymbol{k_e}) \Leftrightarrow G(\boldsymbol{k}-\boldsymbol{k_e})\,. \quad (17)$$

The HARP technique applies a bandpass filter centered on one of the harmonic peaks in k-space created by the cosine modulation (Figure 6). The filter is designed to pass frequency and phase components

associated with the harmonic peak, and remove signal from other sources (such as T_1 relaxation). The Fourier transform of this filtered signal is called the harmonic image. The phase of this complex image, expressed as an angle in the range $[-\pi,\pi)$, is called the harmonic phase. This phase encodes the original position **X** at each current position **x**, and can be thought of as being fixed with respect to material coordinates: as the heart deforms the harmonic phase of a material point is constant.

A Fourier shift operator can be used shift the filtered k-space harmonic peak back to the origin of k-space (i.e. a convolution in k-space with $\delta(\mathbf{k}-\mathbf{k}_e)$: a delta function at $\mathbf{k}_e$). This has the effect of multiplying the harmonic image by $\exp(j\mathbf{k}_e.\mathbf{x})$, giving

$$H(\mathbf{x}) = \frac{M_0(\mathbf{X}(\mathbf{x}))}{2}\left(\exp(j\mathbf{k}_e \cdot (\mathbf{x}-\mathbf{X}))\right). \quad (18)$$

which is an image whose phase is proportional to displacement. The phase is wrapped into the range $[-\pi,\pi)$ and requires unwrapping procedures to recover the true displacement.

The spatial resolution of the harmonic phase is determined by the size of the filter used to isolate the spectral peak. It is therefore desirable to increase the size of the filter as much as possible [97]. Kuijer *et al.* [97] noted that a 1-1 CSPAMM tagging procedure allows cancellation of the relaxed component, which enables the size of the filter to be increased, resulting in a higher resolution displacement map.

DENSE: The displacement of tissue between two time points can be directly encoded into the phase of the MRI signal using methods similar to those used to obtain phase contrast velocity measurements (Figure 5). Initially thought to be too limited by signal loss [98], a feasible implementation was introduced by Aletras et al. [99] – termed DENSE (Displacement Encoding with Stimulated Echoes). This method (Figure 7) can be thought of as an initial 1-1 SPAMM preparation pulse sequence followed by a displacement decoding gradient and readout. The effect of the decoding gradient is to add a phase modulation proportional to the current position **x**:

$$M_z = \{M_0(1-\exp(-t/T1)) + M_0\cos(\boldsymbol{k_e}\cdot\boldsymbol{X})\exp(-t/T1)\}\exp(-j\boldsymbol{k_e}\cdot\boldsymbol{x}) \quad (19)$$

According to the Fourier shift theorem, the effect of the decoding gradient is to shift the spectral peaks by $\mathbf{k}_e$ in k-space. The signal can be considered as arising from three terms:

$$\begin{aligned} M_{xy}(\mathbf{x},t) = &\frac{M_0}{2}\exp(-t/T1)\exp(-j\mathbf{k}_e\cdot(\mathbf{x}-\mathbf{X})) \\ &+ M_0(1-\exp(-t/T1))\exp(-j\mathbf{k}_e\cdot\mathbf{x}) \\ &+ \frac{M_0}{2}\exp(-t/T1)\exp(-j\mathbf{k}_e\cdot(\mathbf{x}+\mathbf{X})). \end{aligned} \quad (20)$$

The first component is the desired DENSE signal, whose phase is directly proportional to the tissue displacement **u**. The second component arises out of the T_1 relaxation and has a phase modulated by the spatial position **x**. The third component has a phase modulated by **x**+**X**, i.e. a complex sinusoid which varies approximately twice as fast as the initial tag frequency. These three signal components give rise to spectral peaks in k space at 0, $\mathbf{k}_e$ and $2\mathbf{k}_e$ respectively. The tag gradient $\mathbf{k}_e$ can be chosen to high enough so that the third spectral peak is shifted above the maximum frequency sampled (Figure 7). (The spatial frequencies above twice the sampling frequency are removed with an analog low pass filter before the signal is sampled, so that the higher spatial frequencies will not be aliased into the digitized signal.)

The second term, arising due to T_1 relaxation, has a phase modulated by $\mathbf{k}_e\cdot\mathbf{x}$. This term cannot be pushed out of the readout window because large values of $\mathbf{k}_e$ result in unacceptable signal loss due to myocardial strain. Instead, the CSPAMM technique can be used to subtract out the relaxed component. As in CSPAMM HARP, two data sets are acquired, in which the second RF pulse in the 1-1 SPAMM encoding is +90 in the first set and –90 in the second set. Subtraction of these two images reinforces the first term and cancels out the second term [66].

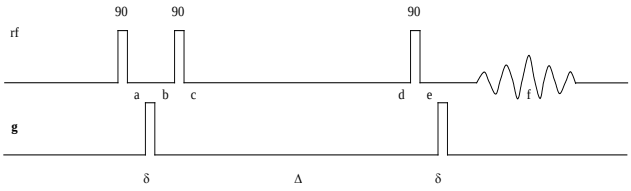

a

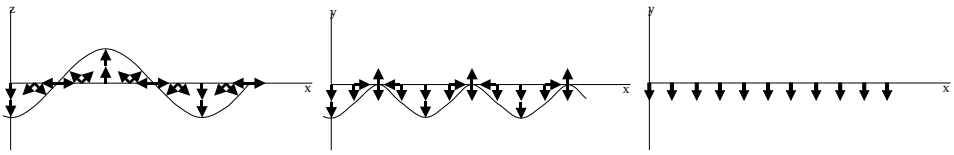

b c d

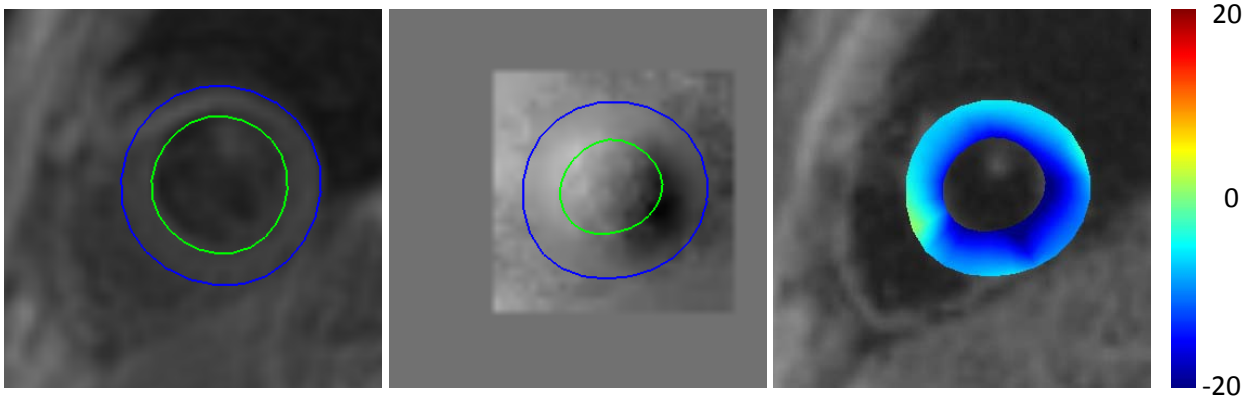

e f g

Figure 7. DENSE. a) Stimulated echo pulse sequence. b) Euler representation as the sum of two complex phasors. c) Transverse magnetization after application of the decoding gradient. d) Displacement encoded signal after application of an analog low pass filter to remove the signal oscillating at ~2k_e. e) Magnitude DENSE image at end-diastole with left ventricular contours. f)

Unwrapped phase for x displacement. g) Circumferential strain at end-systole. Embedded video shows animation of dense displacements and circumferential strain.

It is interesting to note that DENSE pulse sequence is the stimulated echo version of the velocity phase contrast sequence (Figure 5), which is also used to quantify diffusion through signal loss (Figure 4). A similar sequence has been used to measure diffusion in the beating heart [60]. However, DENSE is also strain weighted, since any strain within the tissue will also cause dephasing within a voxel and subsequent loss in signal. This was exploited by Osman *et al.* [67], who used the signal difference between two acquisitions with different through-plane encoding gradients to estimate strain in the direction normal to the slice. Relative through-plane displacement was determined from the phase. In theory, strain encoded imaging (SENC) could be used to estimate all components of the strain tensor, using at least 6 different displacement encoding directions and many encoding strengths, to obtain a strain spectrum at each voxel in a similar manner to MR diffusion tensor imaging.

Strain Estimation: Strain and deformation components can be calculated from each of the MRI displacement encoding methods, using a generalized analysis framework. In each method, displacement can be calculated at each pixel, either from SPAMM tagging using non-rigid registration, from HARP using unwrapped displacement maps, or from DENSE using unwrapped displacement maps. In all these methods the slice and pixel position remains fixed whereas myocardial material points move through the image, and displacement or reference position is given at each current pixel. It is therefore advantageous to employ an Eulerian deformation map **X**(**x**). Strain can be simply calculated from the deformation gradients:

$$H_{ij} = \frac{\partial X_i}{\partial x_j} \tag{21}$$

The Eulerian (or Almansi's) strain tensor *e* is given by

$$e = \frac{1}{2}\left(I - H^T H \right) \quad (22)$$

However it is more common to report strain in Lagrangian form as a change through time from a single reference state. Given a Lagrangian deformation map **x**(**X**) the deformation gradients are

$$F_{ij} = \frac{\partial x_i}{\partial X_j} \quad (23)$$

The Lagrangian (or Green's) strain tensor *E* is given by

$$E = \frac{1}{2}\left(F^T F - I\right) \quad (24)$$

Each of these strain representations has limitations, for example the Lagrangian strain is bounded below by -0.5, whereas the Eulerian strain is bounded above by +0.5. It is still unclear which strain measure is best for the evaluation of cardiac disease. One promising measure is the natural or logarithmic strain ln(e) which is not bounded [100]. Deformations may be linearly decomposable in Log-Euclidean space, enabling a choice of different basis functions for deformation which may lend themselves to dimension reduction techniques such as principal component analysis [101].

Strain in Biomechanics. The methods described above have been used to examine regional strain in a variety of cardiac diseases, including hypertrophic cardiomyopathy [9], aortic stenosis [102], hypertension [103], ischemia [104] infarction [105], mouse models of cardiac disease [106], diastolic dysfunction [107] [108] and asymptomatic pre-clinical pathology [109]. In particular, the quantification of left ventricular torsion, which can be computed from displacement measurements, provides important information on myocardial mechanics over and above standard pump function. Mathematical models, which solve the Newtonian equations of motion in a continuum stress balance, have shown that the normal distribution of myofiber orientation in healthy subjects equilibrates fiber contraction and fiber stress across the wall, so that myocytes contract uniformly from epicardium to endocardium

[110,111]. Torsion is markedly different in conditions where the myofiber architecture is not normal. For example, in situs inversus totalis, the apical and epicardial basal fiber orientation is normal but the deeper basal fibers have an inverted fiber orientation. Torsion is consequently normal at the apex but changes sign towards the base [112].

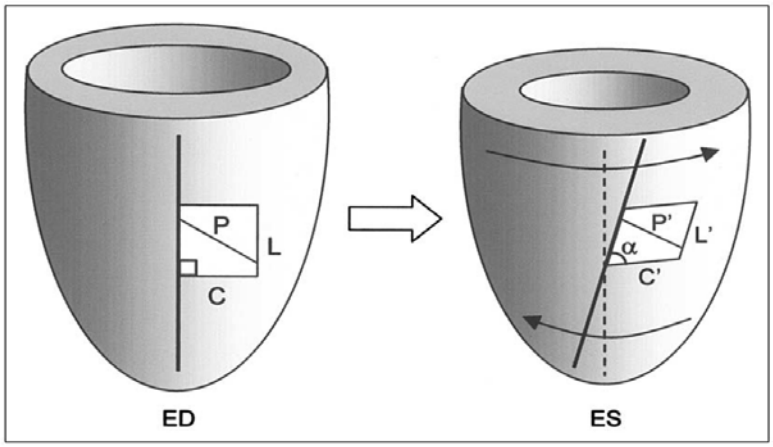

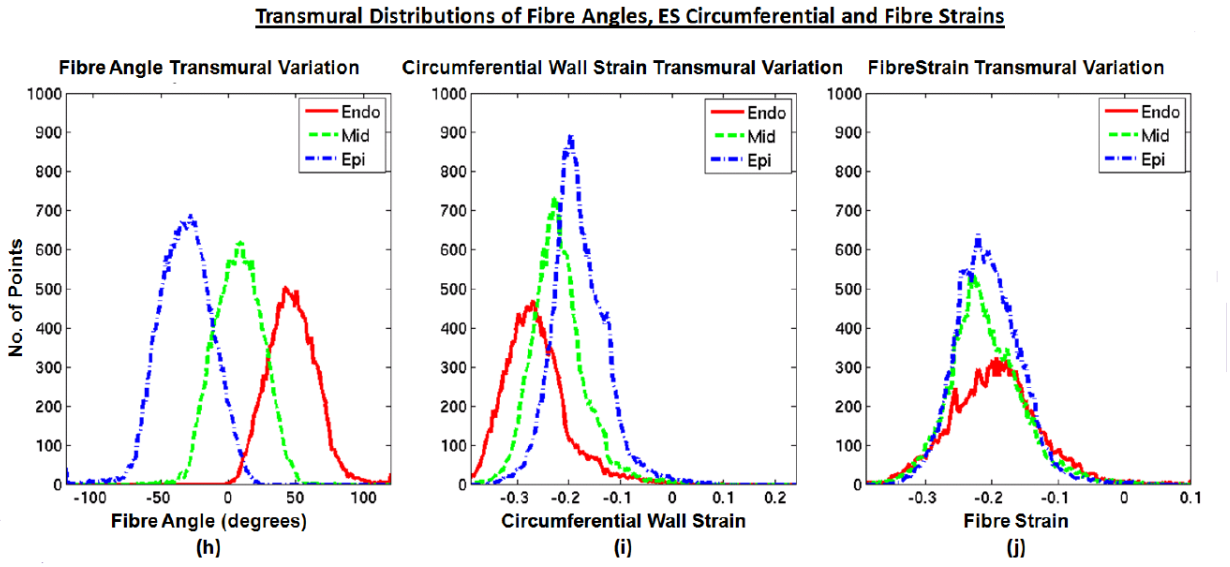

Figure 8. Three dimensional strain in the left ventricle. a) Circumferential (C->C') and longitudinal (L-L') contraction during systole is accompanied by radial thickening (not shown), and torsion (arrows and a). Maximal shortening (P->P') is oriented obliquely [10]. b) Histograms of fiber direction (left)

circumferential strain (middle) and fiber strain (right). Although circumferential strain is higher towards the endocardium, fibre strain is approximately uniform transmurally. [113]

Mathematical models have shown that a specific relationship between torsion and ejection is required to balance forces and maintain a uniform fiber shortening across the wall [114]. This leads to a constant ratio between shortening and torsion during systole across mammalian species, known as the torsion-to-shortening ratio (TSR) [102], which is theoretically independent of contractility, afterload, and preload. Changes in this ratio therefore indicate transmural differences in fiber contraction. TSR has been shown to be substantially increased in patients with aortic stenosis [102] with smaller increases seen in normal aging [115]. Recently, Russel et al. [116] found increased torsion and TSR in HCM mutation carriers with normal wall thickness, perhaps indicating preclinical subendocardial dysfunction.

The substantial wall thickening which occurs during systole cannot be solely due to myocyte thickening, so substantial shear deformations must act to facilitate wall thickening, and therefore pump function. These transverse shears are mechanically facilitated by myocardial laminae and maximum local shearing is aligned with the laminae orientation in the subendocardium [117-119]. One source of transverse shear is due to a difference in rotational motion between epicardium and endocardium (circumferential-radial shear). MRI tagging studies have shown that the endocardium rotates more anticlockwise at the apex while at the base the endocardium rotates more clockwise than the epicardium [9]. This increase in torsion towards the endocardium gives rise to a characteristic circumferential-radial shear pattern which varies longitudinally from positive in the apex to negative in the base, passing through zero in the middle [9]. This is paradoxical since subendocardial fibers mechanically reduce torsion at the subendocardium, not increase it. One possible mechanism may be the existence of transverse myocardial fibers which can more effectively transmit epicardial forces to the endocardium [120]. Although there is some evidence

of transverse angle from DTMRI [121], whether this is sufficient to account for the observed transverse shear is not yet known.

Imaging strain in combination with DTI will yield insights in to the influence of structure on function. Wu *et al.* [64,72] found that the magnitude of circumferential strain was negatively correlated with right-handed fibers, whilst positively correlated with left-handed fibers. The mechanism for this relationship is currently unknown.

Atlases

The noninvasive, tomographic, 3D, time-resolved nature of MRI lends itself to creating integrative statistical atlases of cardiac function. Although well-established for the brain [122], statistical maps of regional cardiac shape and function are only recently being developed. The ability to integrate multi-source, multivariate data has enormous implications for the diagnosis and clinical care of patients [123]. Mathematical and computational models can be combined with large scale population databases in a standardized way, providing both a statistical map of the variation seen in heart disease as well as highly detailed information which can be used to characterize function in an individual patient (patient specific models) [124]. These models can elucidate the complex interaction of electrical, anatomical, and functional data to provide insight into the processes underlying the normal or pathological function of the heart. Furthermore, models derived from large populations of patients can provide a range of reference values against which individual patients' data can be compared. One study, the Cardiac Atlas Project (CAP), has combined data from several sources to construct registered maps of regional cardiac function [125]. Data sharing mechanisms have been established by which large scale cardiac imaging datasets can be classified, annotated and shared in a HIPAA compliant manner via a web-accessible interface with the cardiac research community. These statistical atlases of shape and function enable automatic characterization of regional wall motion abnormalities [126]. The database contains over

3000 cardiac MRI imaging examinations (approximately 1.5 million images) have been contributed into the CAP database, with the majority of examinations contributed from large research studies such as the Multi-Ethnic Study of Atherosclerosis (MESA) [20], and clinical studies such as the Defibrillators to Reduce Risk by Magnetic Resonance Imaging Evaluation (DETERMINE) study [127]. Annotations and associated metadata are performed using a controlled vocabulary, using terms from SNOMED-CT [128] the Foundational Model of Anatomy (FMA) [129], as well as the RadLex [130].

A standardized model-based analysis can be used to establish shape and motion with respect to a standard coordinate system, similar to the Talairach coordinate system used in the brain [131] [132]. Since shape and motion are mathematically mapped, statistical tools such as principal component analysis can be used to quantify the significant modes of variation present within a population. For example, the major modes of variation within a subset of the DETERMINE cohort were calculated using a principal component analysis (Figure 9): The first three modes associated with the greatest variation were found to correspond with size, sphericity, and mitral valve geometry. These results are encouraging since each of these modes is known to be associated with adverse geometric remodeling following myocardial infarction. Projection of an individual's shape and motion onto these modes (e.g., sphericity) provides a standardized method for quantifying the amount of each mode present.

Data sharing is vital tool for the development of the field and many researchers are making datasets available to the community for benchmarking and algorithm development, including electrophysiological data for simulating heart activation, tagging, and echocardiographic data for the reconstruction of motion, flow data for computational fluid dynamics, and late gadolinium enhancement data for the quantification of scar in the atria and ventricles [133] [134].

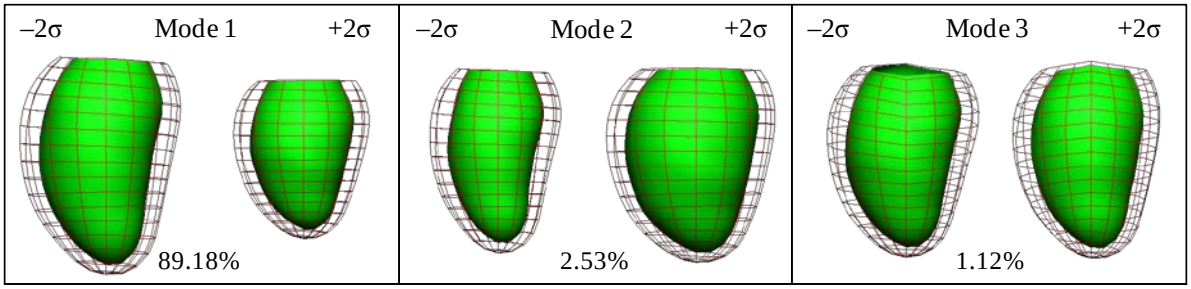

Figure 9: Principal component analysis of shape variation in patients with myocardial infarction (n=200). The first three modes are associated with size (left), sphericity (middle) and mitral annulus geometry (right). Embedded video shows animation of +/- two standard deviations in the most dominant shape modes [125].

Computational Physiology

Computational models of cardiac mechanics can give insight into the pathophysiological processes underlying heart disease. By combining measurements of geometry, microstructure, and strain from MRI with pressure recordings or estimates from applanation tonometry or flow, mechanical models can predict local stress and energy expenditure [135]. Finite element analysis incorporating nonlinear anisotropic constitutive properties and active tension generation can be customized to a patient specific geometry, motion and boundary conditions, enabling the estimation of material parameters including passive stiffness and contractility [136]. Conservation of momentum (assuming quasi-static equilibrium) gives rise to the stress equilibrium:

$$\frac{\partial}{\partial X_m}\left(T^{MN}\frac{\partial x_j}{\partial X_N}\right)=0 \qquad (25)$$

The principle of virtual work relates boundary forces to the internal stress field:

$$\int_V T^{MN} \frac{1}{J} \frac{\partial x_j}{\partial X_M} \frac{\partial \delta v_j}{\partial X_N} dV = \int_{S_2} s \cdot \delta v dS \tag{26}$$

The large strain hyperelastic stress-strain relationships govern the passive and active components of tension:

$$T^{MN} = \frac{1}{2}\left(\frac{\partial W}{\partial E_{MN}} + \frac{\partial W}{\partial E_{NM}} \right) - p \frac{\partial X_M}{\partial x_k} \frac{\partial X_N}{\partial x_k} + T_a \delta_1^M \delta_1^N \tag{27}$$

where T_a is the active tension generated in the direction of the myocytes [137]. The form of the passive and active material laws is currently an open question. Several authors have used the transversely-isotropic Fung exponential form (Guccione):

$$\begin{aligned} W &= C_1 \exp(Q) \\ Q &= C_2 E_{ff}^2 + C_3 (E_{cc}^2 + E_{rr}^2 + E_{cr} E_{rc}) + 2C_4 (E_{fc} E_{cf} + E_{fr} E_{rf}) \end{aligned} \tag{28}$$

where $E_{\alpha\beta}$ are the components of Green's (Lagrange) strain tensor referred to fibre (*f*), cross-fibre (*c*), and radial (*r*) coordinates. C_1 - C_4 are the myocardial constitutive parameters and are tuned to match the model predicted motions of the set of 3D material points derived from MRI tagging.

At present there are two main approaches to this inverse problem. A variational formulation of the equations of elasticity leads to a Galerkin finite element solution for stress given an estimate for the material properties. Nonlinear optimization methods are used to find the optimal solution for the material properties which best matches the imaging data and boundary conditions [58] [135]. Alternatively state space data assimilation methods can be used to estimate the material parameters. Kalman filtering approaches have been adapted to achieve tractable nonlinear estimators to solve the joint state-parameter estimation problem [138] [139]. Xi *et al.* [140] demonstrated an unscented Kalman

filter estimation of the Guccione material parameters. Local contractility was estimated by Sermesant *et al.* [141].

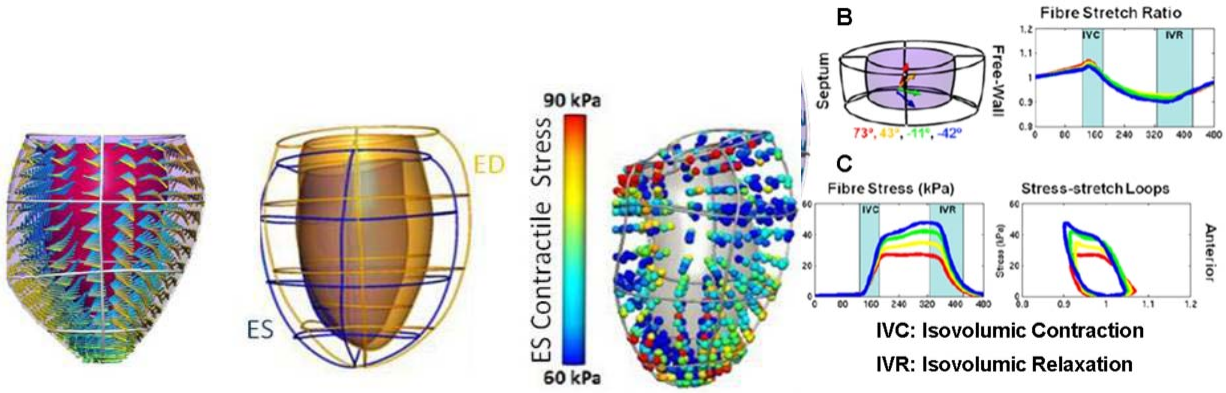

a b c d

Figure 10. Customized structural model (left) of the LV to analyze mechanics (middle) and regional myocardial contractile function (right). a) Nonlinear anisotropic finite element model with fibre angles showing variation from epicardium to endocardium. b) Fiber stretch at different transmural locations in the midventricle. c) Stress and stress-stretch estimated from calculated hyperelastic material properties in a canine heart [137] [142].

A current problem is that it is difficult to uniquely identify all the parameters of current material laws using imaging data, since the strain is dependent on several parameters and the covariance matrix arising from the estimation problem is often poorly conditioned [58]. Constitutive laws which are more tightly coupled to the pathology undergone in cardiac disease, for example with structurally motivated parameters [136,143], and material law formulations which are better posed in terms of parameter identifiability [144] will be highly beneficial in discriminating patients on the basis of the underlying

pathology. This will highlight pathways to target treatment, particularly in patients with NFNEF for whom existing treatments are ineffective.

Conclusions and Future work

Currently, CMR has a number of well established methods for the examination of biomechanics in health and disease. SSFP imaging is the standard for evaluation of morphology and pump function and is particularly useful in children with congenital heart disease. Blood flow dynamics are readily quantified in the great vessels with 4Dflow methods. Tissue motion and regional strain can be quantified with displacement encoding methods. T_1 and T_2 mapping can be used to examine edema and extracellular volume fraction.

A number of techniques have been demonstrated in theory or in animal studies, such as T_1 mapping, but still require further investigation in order to translate the findings to humans. Myocardial stiffness and contractility quantified using computational physiology methods needs to be applied to heart failure patients with preserved and reduced ejection fraction [145]. Elastography techniques may enable quantification of dynamic stiffness parameters in heart failure patients. The mechanisms for transverse shears and their alterations during disease need to be examined. Other methods, such as strain imaging, are well established but still require optimization in clinical settings. For example, it is still unclear which displacement encoding method is optimal in patients. This evaluation should be performed with a standardized analysis framework so that the relative advantages or disadvantages of the imaging methods can be examined without bias due to the processing method [146].

On the horizon, a number of techniques show great promise but still require substantial research and development. Diffusion tensor imaging *in vivo* will enable examination of myofiber architecture in disease [72]. Compressed sensing methods may enable much faster acquisition of CMR data, but require efficient reconstruction algorithms [147]. Better imaging methods are required to examine the coronary

arteries to give similar quality to CT. The fusion of modalities, such as imaging coronary arteries from CT, perfusion from MRI, and metabolism from PET, may provide useful integration of information and lead to enhanced diagnostic and prognostic capabilities. Population studies and data sharing and standardization show great promise in meta-analyses across patient groups [125]. On the whole, cardiovascular magnetic resonance imaging currently provides a wealth of information about the heart and the potential for future developments is great.

References

1. **Rosamond W, Flegal K, Furie K, Go A, Greenlund K, Haase N, Hailpern SM, Ho M, Howard V, Kissela B, Kittner S, Lloyd-Jones D, McDermott M, Meigs J, Moy C, Nichol G, O'Donnell C, Roger V, Sorlie P, Steinberger J, Thom T, Wilson M, Hong Y. Heart disease and stroke statistics--2008 update: a report from the American Heart Association Statistics Committee and Stroke Statistics Subcommittee. Circulation 2008;117:e25-146**
2. **Borlaug BA, Redfield MM. Diastolic and systolic heart failure are distinct phenotypes within the heart failure spectrum. Circulation 2011;123:2006-2013; discussion 2014**
3. **De Keulenaer GW, Brutsaert DL. Systolic and diastolic heart failure are overlapping phenotypes within the heart failure spectrum. Circulation 2011;123:1996-2004; discussion 2005**
4. **Lam CS, Donal E, Kraigher-Krainer E, Vasan RS. Epidemiology and clinical course of heart failure with preserved ejection fraction. Eur J Heart Fail 2011;13:18-28**
5. **Owan TE, Hodge DO, Herges RM, Jacobsen SJ, Roger VL, Redfield MM. Trends in prevalence and outcome of heart failure with preserved ejection fraction. N Engl J Med 2006;355:251-259**
6. **Al-Mohammad A, Mant J, Laramee P, Swain S. Diagnosis and management of adults with chronic heart failure: summary of updated NICE guidance. BMJ 2012;341:c4130**
7. **Reichek N. Magnetic resonance imaging for assessment of myocardial function. Magn Reson Q 1991;7:255-274**
8. **Pattynama PM, De Roos A, Van der Wall EE, Van Voorthuisen AE. Evaluation of cardiac function with magnetic resonance imaging. Am Heart J 1994;128:595-607**
9. **Young AA, Kramer CM, Ferrari VA, Axel L, Reichek N. Three-dimensional left ventricular deformation in hypertrophic cardiomyopathy. Circulation 1994;90:854-867**
10. **Fonseca CG, Dissanayake AM, Doughty RN, Whalley GA, Gamble GD, Cowan BR, Occleshaw CJ, Young AA. Three-dimensional assessment of left ventricular systolic strain in patients with**

type 2 diabetes mellitus, diastolic dysfunction, and normal ejection fraction. Am J Cardiol 2004;94:1391-1395

11. Hsu EW, Muzikant AL, Matulevicius SA, Penland RC, Henriquez CS. Magnetic resonance myocardial fiber-orientation mapping with direct histological correlation. Am J Physiol 1998;274:H1627-1634
12. Scollan DF, Holmes A, Winslow R, Forder J. Histological validation of myocardial microstructure obtained from diffusion tensor magnetic resonance imaging. Am J Physiol 1998;275:H2308-2318
13. Kilner PJ, Yang GZ, Wilkes AJ, Mohiaddin RH, Firmin DN, Yacoub MH. Asymmetric redirection of flow through the heart. Nature 2000;404:759-761
14. Panting JR, Gatehouse PD, Yang GZ, Grothues F, Firmin DN, Collins P, Pennell DJ. Abnormal subendocardial perfusion in cardiac syndrome X detected by cardiovascular magnetic resonance imaging. N Engl J Med 2002;346:1948-1953
15. Kim RJ, Wu E, Rafael A, Chen EL, Parker MA, Simonetti O, Klocke FJ, Bonow RO, Judd RM. The use of contrast-enhanced magnetic resonance imaging to identify reversible myocardial dysfunction. N Engl J Med 2000;343:1445-1453
16. Wagner A, Mahrholdt H, Holly TA, Elliott MD, Regenfus M, Parker M, Klocke FJ, Bonow RO, Kim RJ, Judd RM. Contrast-enhanced MRI and routine single photon emission computed tomography (SPECT) perfusion imaging for detection of subendocardial myocardial infarcts: an imaging study. Lancet 2003;361:374-379
17. Pattynama PM, Lamb HJ, Van der Velde EA, Van der Geest RJ, Van der Wall EE, De Roos A. Reproducibility of MRI-derived measurements of right ventricular volumes and myocardial mass. Magn Reson Imaging 1995;13:53-63
18. Geva T. Repaired tetralogy of Fallot: the roles of cardiovascular magnetic resonance in evaluating pathophysiology and for pulmonary valve replacement decision support. J Cardiovasc Magn Reson 2011;13:9
19. Myerson SG, Bellenger NG, Pennell DJ. Assessment of left ventricular mass by cardiovascular magnetic resonance. Hypertension 2002;39:750-755
20. Bild DE, Bluemke DA, Burke GL, Detrano R, Diez Roux AV, Folsom AR, Greenland P, Jacob DR, Jr., Kronmal R, Liu K, Nelson JC, O'Leary D, Saad MF, Shea S, Szklo M, Tracy RP. Multi-ethnic study of atherosclerosis: objectives and design. Am J Epidemiol 2002;156:871-881
21. Pitcher A, Ashby D, Elliott P, Petersen SE. Cardiovascular MRI in clinical trials: expanded applications through novel surrogate endpoints. Heart 2011;97:1286-1292
22. Carr JC, Simonetti O, Bundy J, Li D, Pereles S, Finn JP. Cine MR angiography of the heart with segmented true fast imaging with steady-state precession. Radiology 2001;219:828-834
23. Fieno DS, Jaffe WC, Simonetti OP, Judd RM, Finn JP. TrueFISP: assessment of accuracy for measurement of left ventricular mass in an animal model. J Magn Reson Imaging 2002;15:526-531
24. Germain P, Roul G, Kastler B, Mossard JM, Bareiss P, Sacrez A. Inter-study variability in left ventricular mass measurement. Comparison between M-mode echography and MRI. Eur Heart J 1992;13:1011-1019
25. Kuehne T, Yilmaz S, Steendijk P, Moore P, Groenink M, Saaed M, Weber O, Higgins CB, Ewert P, Fleck E, Nagel E, Schulze-Neick I, Lange P. Magnetic resonance imaging analysis of right ventricular pressure-volume loops: in vivo validation and clinical application in patients with pulmonary hypertension. Circulation 2004;110:2010-2016
26. Petitjean C, Dacher JN. A review of segmentation methods in short axis cardiac MR images. Med Image Anal 2011;15:169-184

27. Bloomer TN, Plein S, Radjenovic A, Higgins DM, Jones TR, Ridgway JP, Sivananthan MU. Cine MRI using steady state free precession in the radial long axis orientation is a fast accurate method for obtaining volumetric data of the left ventricle. J Magn Reson Imaging 2001;14:685-692
28. Rogers WJ, Jr., Shapiro EP, Weiss JL, Buchalter MB, Rademakers FE, Weisfeldt ML, Zerhouni EA. Quantification of and correction for left ventricular systolic long-axis shortening by magnetic resonance tissue tagging and slice isolation. Circulation 1991;84:721-731
29. Young AA, Cowan BR, Thrupp SF, Hedley WJ, Dell'Italia LJ. Left ventricular mass and volume: fast calculation with guide-point modeling on MR images. Radiology 2000;216:597-602
30. Hung J, Francois C, Nelson NA, Young A, Cowan BR, Jerecic R, Carr J. Cardiac image modeling tool for quantitative analysis of global and regional cardiac wall motion. Invest Radiol 2009;44:271-278
31. Li B, Liu Y, Occleshaw CJ, Cowan BR, Young AA. In-line automated tracking for ventricular function with magnetic resonance imaging. JACC Cardiovasc Imaging 2010;3:860-866
32. Chan J, Khafagi F, Young AA, Cowan BR, Thompson C, Marwick TH. Impact of coronary revascularization and transmural extent of scar on regional left ventricular remodelling. Eur Heart J 2008;29:1608-1617
33. Chalil S, Stegemann B, Muhyaldeen S, Khadjooi K, Smith RE, Jordan PJ, Leyva F. Intraventricular dyssynchrony predicts mortality and morbidity after cardiac resynchronization therapy: a study using cardiovascular magnetic resonance tissue synchronization imaging. J Am Coll Cardiol 2007;50:243-252
34. Mewton N, Liu CY, Croisille P, Bluemke D, Lima JA. Assessment of myocardial fibrosis with cardiovascular magnetic resonance. J Am Coll Cardiol 2011;57:891-903
35. Jerosch-Herold M. Quantification of myocardial perfusion by cardiovascular magnetic resonance. J Cardiovasc Magn Reson 2010;12:57
36. Gerber BL, Raman SV, Nayak K, Epstein FH, Ferreira P, Axel L, Kraitchman DL. Myocardial first-pass perfusion cardiovascular magnetic resonance: history, theory, and current state of the art. J Cardiovasc Magn Reson 2008;10:18
37. Jerosch-Herold M, Hu X, Murthy NS, Rickers C, Stillman AE. Magnetic resonance imaging of myocardial contrast enhancement with MS-325 and its relation to myocardial blood flow and the perfusion reserve. J Magn Reson Imaging 2003;18:544-554
38. Axel L. Tissue mean transit time from dynamic computed tomography by a simple deconvolution technique. Invest Radiol 1983;18:94-99
39. Hsu LY, Groves DW, Aletras AH, Kellman P, Arai AE. A quantitative pixel-wise measurement of myocardial blood flow by contrast-enhanced first-pass CMR perfusion imaging: microsphere validation in dogs and feasibility study in humans. JACC Cardiovasc Imaging 2012;5:154-166
40. Zhang H, Shea SM, Park V, Li D, Woodard PK, Gropler RJ, Zheng J. Accurate myocardial T1 measurements: toward quantification of myocardial blood flow with arterial spin labeling. Magn Reson Med 2005;53:1135-1142
41. Arnold JR, Karamitsos TD, Bhamra-Ariza P, Francis JM, Searle N, Robson MD, Howells RK, Choudhury RP, Rimoldi OE, Camici PG, Banning AP, Neubauer S, Jerosch-Herold M, Selvanayagam JB. Myocardial oxygenation in coronary artery disease: insights from blood oxygen level-dependent magnetic resonance imaging at 3 Tesla. J Am Coll Cardiol 2012;59:1954-1964
42. Johansson E, Olsson LE, Mansson S, Petersson JS, Golman K, Stahlberg F, Wirestam R. Perfusion assessment with bolus differentiation: a technique applicable to hyperpolarized tracers. Magn Reson Med 2004;52:1043-1051

43. Kim RJ, Fieno DS, Parrish TB, Harris K, Chen EL, Simonetti O, Bundy J, Finn JP, Klocke FJ, Judd RM. Relationship of MRI delayed contrast enhancement to irreversible injury, infarct age, and contractile function. Circulation 1999;100:1992-2002
44. Orn S, Manhenke C, Anand IS, Squire I, Nagel E, Edvardsen T, Dickstein K. Effect of left ventricular scar size, location, and transmurality on left ventricular remodeling with healed myocardial infarction. Am J Cardiol 2007;99:1109-1114
45. Kwon DH, Smedira NG, Rodriguez ER, Tan C, Setser R, Thamilarasan M, Lytle BW, Lever HM, Desai MY. Cardiac magnetic resonance detection of myocardial scarring in hypertrophic cardiomyopathy: correlation with histopathology and prevalence of ventricular tachycardia. J Am Coll Cardiol 2009;54:242-249
46. Krittayaphong R, Boonyasirinant T, Chaithiraphan V, Maneesai A, Saiviroonporn P, Nakyen S, Thanapiboonpol P, Yindeengam A, Udompanturak S. Prognostic value of late gadolinium enhancement in hypertensive patients with known or suspected coronary artery disease. Int J Cardiovasc Imaging 2010;26 Suppl 1:123-131
47. Kwong RY, Sattar H, Wu H, Vorobiof G, Gandla V, Steel K, Siu S, Brown KA. Incidence and prognostic implication of unrecognized myocardial scar characterized by cardiac magnetic resonance in diabetic patients without clinical evidence of myocardial infarction. Circulation 2008;118:1011-1020
48. Messroghli DR, Radjenovic A, Kozerke S, Higgins DM, Sivananthan MU, Ridgway JP. Modified Look-Locker inversion recovery (MOLLI) for high-resolution T1 mapping of the heart. Magn Reson Med 2004;52:141-146
49. Iles L, Pfluger H, Phrommintikul A, Cherayath J, Aksit P, Gupta SN, Kaye DM, Taylor AJ. Evaluation of diffuse myocardial fibrosis in heart failure with cardiac magnetic resonance contrast-enhanced T1 mapping. J Am Coll Cardiol 2008;52:1574-1580
50. Messroghli DR, Nordmeyer S, Dietrich T, Dirsch O, Kaschina E, Savvatis K, D Oh-I, Klein C, Berger F, Kuehne T. Assessment of diffuse myocardial fibrosis in rats using small-animal Look-Locker inversion recovery T1 mapping. Circ Cardiovasc Imaging 2011;4:636-640
51. Flett AS, Hayward MP, Ashworth MT, Hansen MS, Taylor AM, Elliott PM, McGregor C, Moon JC. Equilibrium contrast cardiovascular magnetic resonance for the measurement of diffuse myocardial fibrosis: preliminary validation in humans. Circulation 2010;122:138-144
52. Arheden H, Saeed M, Higgins CB, Gao DW, Bremerich J, Wyttenbach R, Dae MW, Wendland MF. Measurement of the distribution volume of gadopentetate dimeglumine at echo-planar MR imaging to quantify myocardial infarction: comparison with 99mTc-DTPA autoradiography in rats. Radiology 1999;211:698-708
53. Ugander M, Oki AJ, Hsu LY, Kellman P, Greiser A, Aletras AH, Sibley CT, Chen MY, Bandettini WP, Arai AE. Extracellular volume imaging by magnetic resonance imaging provides insights into overt and sub-clinical myocardial pathology. Eur Heart J 2012;33:1268-1278
54. Ugander M, Bagi PS, Oki AJ, Chen B, Hsu LY, Aletras AH, Shah S, Greiser A, Kellman P, Arai AE. Myocardial edema as detected by pre-contrast T1 and T2 CMR delineates area at risk associated with acute myocardial infarction. JACC Cardiovasc Imaging 2012;5:596-603
55. Coelho-Filho O, Mitchell RN, Moreno H, Kwong R, Jerosch-Herold M. MRI based non-invasive detection of cardiomyocyte hypertrophy and cell-volume changes. Journal of Cardiovascular Magnetic Resonance 2012;14:O10
56. Callaghan PT. Principles of nuclear magnetic resonance microscopy.: Oxford University Press; 1991
57. Basser PJ, Mattiello J, LeBihan D. MR diffusion tensor spectroscopy and imaging. Biophys J 1994;66:259-267

58. Augenstein KF, Cowan BR, LeGrice IJ, Nielsen PM, Young AA. Method and apparatus for soft tissue material parameter estimation using tissue tagged Magnetic Resonance Imaging. J Biomech Eng 2005;127:148-157
59. Sosnovik DE, Wang R, Dai G, Wang T, Aikawa E, Novikov M, Rosenzweig A, Gilbert RJ, Wedeen VJ. Diffusion spectrum MRI tractography reveals the presence of a complex network of residual myofibers in infarcted myocardium. Circ Cardiovasc Imaging 2009;2:206-212
60. Dou J, Tseng WY, Reese TG, Wedeen VJ. Combined diffusion and strain MRI reveals structure and function of human myocardial laminar sheets in vivo. Magn Reson Med 2003;50:107-113
61. Sosnovik DE, Wang R, Dai G, Reese TG, Wedeen VJ. Diffusion MR tractography of the heart. J Cardiovasc Magn Reson 2009;11:47
62. Gilbert SH, Benson AP, Li P, Holden AV. Regional localisation of left ventricular sheet structure: integration with current models of cardiac fibre, sheet and band structure. Eur J Cardiothorac Surg 2007;32:231-249
63. Nielles-Vallespin S, Mekkaoi C, Gatehouse PD, Reese TG, Keegan J, Collins S, Speier P, Feiweier T, Jackowski MP, Sosnovik DE, Firmin DN. Diffusion tensor MRI of the human heart In Vivo with a navigator based free breathing approach Journal of Cardiovascular Magnetic Resonance 2012;14:238
64. Wu MT, Tseng WY, Su MY, Liu CP, Chiou KR, Wedeen VJ, Reese TG, Yang CF. Diffusion tensor magnetic resonance imaging mapping the fiber architecture remodeling in human myocardium after infarction: correlation with viability and wall motion. Circulation 2006;114:1036-1045
65. Tseng WY, Reese TG, Weisskoff RM, Wedeen VJ. Cardiac diffusion tensor MRI in vivo without strain correction. Magn Reson Med 1999;42:393-403
66. Kim D, Gilson WD, Kramer CM, Epstein FH. Myocardial tissue tracking with two-dimensional cine displacement-encoded MR imaging: development and initial evaluation. Radiology 2004;230:862-871
67. Osman NF, Sampath S, Atalar E, Prince JL. Imaging longitudinal cardiac strain on short-axis images using strain-encoded MRI. Magn Reson Med 2001;46:324-334
68. Chen J, Song SK, Liu W, McLean M, Allen JS, Tan J, Wickline SA, Yu X. Remodeling of cardiac fiber structure after infarction in rats quantified with diffusion tensor MRI. Am J Physiol Heart Circ Physiol 2003;285:H946-954
69. Wu EX, Wu Y, Nicholls JM, Wang J, Liao S, Zhu S, Lau CP, Tse HF. MR diffusion tensor imaging study of postinfarct myocardium structural remodeling in a porcine model. Magn Reson Med 2007;58:687-695
70. Wu Y, Chan CW, Nicholls JM, Liao S, Tse HF, Wu EX. MR study of the effect of infarct size and location on left ventricular functional and microstructural alterations in porcine models. J Magn Reson Imaging 2009;29:305-312
71. Strijkers GJ, Bouts A, Blankesteijn WM, Peeters TH, Vilanova A, van Prooijen MC, Sanders HM, Heijman E, Nicolay K. Diffusion tensor imaging of left ventricular remodeling in response to myocardial infarction in the mouse. NMR Biomed 2009;22:182-190
72. Wu MT, Su MY, Huang YL, Chiou KR, Yang P, Pan HB, Reese TG, Wedeen VJ, Tseng WY. Sequential changes of myocardial microstructure in patients postmyocardial infarction by diffusion-tensor cardiac MR: correlation with left ventricular structure and function. Circ Cardiovasc Imaging 2009;2:32-40, 36 p following 40
73. Markl M, Wallis W, Brendecke S, Simon J, Frydrychowicz A, Harloff A. Estimation of global aortic pulse wave velocity by flow-sensitive 4D MRI. Magn Reson Med 2010;63:1575-1582

74. Bock J, Frydrychowicz A, Stalder AF, Bley TA, Burkhardt H, Hennig J, Markl M. 4D phase contrast MRI at 3 T: effect of standard and blood-pool contrast agents on SNR, PC-MRA, and blood flow visualization. Magn Reson Med 2009;63:330-338
75. Sundareswaran KS, de Zelicourt D, Sharma S, Kanter KR, Spray TL, Rossignac J, Sotiropoulos F, Fogel MA, Yoganathan AP. Correction of pulmonary arteriovenous malformation using image-based surgical planning. JACC Cardiovasc Imaging 2009;2:1024-1030
76. Geiger J, Markl M, Jung B, Grohmann J, Stiller B, Langer M, Arnold R. 4D-MR flow analysis in patients after repair for tetralogy of Fallot. Eur Radiol 2011;21:1651-1657
77. Markl M, Geiger J, Stiller B, Arnold R. Impaired continuity of flow in congenital heart disease with single ventricle physiology. Interact Cardiovasc Thorac Surg 2010;12:87-90
78. O'Brien KR, Cowan BR, Jain M, Stewart RA, Kerr AJ, Young AA. MRI phase contrast velocity and flow errors in turbulent stenotic jets. J Magn Reson Imaging 2008;28:210-218
79. O'Brien KR, Myerson SG, Cowan BR, Young AA, Robson MD. Phase contrast ultrashort TE: A more reliable technique for measurement of high-velocity turbulent stenotic jets. Magn Reson Med 2009;62:626-636
80. Dyverfeldt P, Gardhagen R, Sigfridsson A, Karlsson M, Ebbers T. On MRI turbulence quantification. Magn Reson Imaging 2009;27:913-922
81. Dyverfeldt P, Sigfridsson A, Kvitting JP, Ebbers T. Quantification of intravoxel velocity standard deviation and turbulence intensity by generalizing phase-contrast MRI. Magn Reson Med 2006;56:850-858
82. Arzani A, Dyverfeldt P, Ebbers T, Shadden SC. In vivo validation of numerical prediction for turbulence intensity in an aortic coarctation. Ann Biomed Eng 2011;40:860-870
83. Foell D, Jung B, Germann E, Staehle F, Bode C, Markl M. Hypertensive heart disease: MR tissue phase mapping reveals altered left ventricular rotation and regional myocardial long-axis velocities. Eur Radiol 2012
84. Hennig J, Markl M, Schneider B, Peschl S. Regional myocardial function with tissue phase mapping. MAGMA 1998;6:145-146
85. Wedeen VJ, Weisskoff RM, Reese TG, Beache GM, Poncelet BP, Rosen BR, Dinsmore RE. Motionless movies of myocardial strain-rates using stimulated echoes. Magn Reson Med 1995;33:401-408
86. Axel L, Shimakawa A, MacFall J. A time-of-flight method of measuring flow velocity by magnetic resonance imaging. Magn Reson Imaging 1986;4:199-205
87. Zerhouni EA, Parish DM, Rogers WJ, Yang A, Shapiro EP. Human heart: tagging with MR imaging--a method for noninvasive assessment of myocardial motion. Radiology 1988;169:59-63
88. Axel L, Dougherty L. MR imaging of motion with spatial modulation of magnetization. Radiology 1989;171:841-845
89. Young AA, Kraitchman DL, Dougherty L, Axel L. Tracking and finite element analysis of stripe deformation in magnetic resonance tagging. IEEE Trans Med Imaging 1995;14:413-421
90. Young AA. Model tags: direct three-dimensional tracking of heart wall motion from tagged magnetic resonance images. Med Image Anal 1999;3:361-372
91. Wang X, Chen T, Zhang S, Metaxas D, Axel L. LV motion and strain computation from tMRI based on meshless deformable models. Med Image Comput Comput Assist Interv 2008;11:636-644
92. Dougherty L, Asmuth JC, Blom AS, Axel L, Kumar R. Validation of an optical flow method for tag displacement estimation. IEEE Trans Med Imaging 1999;18:359-363
93. Chandrashekara R, Mohiaddin RH, Rueckert D. Analysis of 3-D myocardial motion in tagged MR images using nonrigid image registration. IEEE Trans Med Imaging 2004;23:1245-1250

94. Ledesma-Carbayo MJ, Derbyshire JA, Sampath S, Santos A, Desco M, McVeigh ER. Unsupervised estimation of myocardial displacement from tagged MR sequences using nonrigid registration. Magn Reson Med 2008;59:181-189
95. Osman NF, Kerwin WS, McVeigh ER, Prince JL. Cardiac motion tracking using CINE harmonic phase (HARP) magnetic resonance imaging. Magn Reson Med 1999;42:1048-1060
96. Osman NF, McVeigh ER, Prince JL. Imaging heart motion using harmonic phase MRI. IEEE Trans Med Imaging 2000;19:186-202
97. Kuijer JP, Jansen E, Marcus JT, van Rossum AC, Heethaar RM. Improved harmonic phase myocardial strain maps. Magn Reson Med 2001;46:993-999
98. Fischer SE, Stuber M, Scheidegger MB, Boesiger P. Limitations of stimulated echo acquisition mode (STEAM) techniques in cardiac applications. Magn Reson Med 1995;34:80-91
99. Aletras AH, Ding S, Balaban RS, Wen H. DENSE: displacement encoding with stimulated echoes in cardiac functional MRI. J Magn Reson 1999;137:247-252
100. Van Der Toorn A, Barenbrug P, Snoep G, Van Der Veen FH, Delhaas T, Prinzen FW, Maessen J, Arts T. Transmural gradients of cardiac myofiber shortening in aortic valve stenosis patients using MRI tagging. Am J Physiol Heart Circ Physiol 2002;283:H1609-1615
101. Arsigny V, Fillard P, Pennec X, Ayache N. Log-Euclidean metrics for fast and simple calculus on diffusion tensors. Magn Reson Med 2006;56:411-421
102. Delhaas T, Kotte J, van der Toorn A, Snoep G, Prinzen FW, Arts T. Increase in left ventricular torsion-to-shortening ratio in children with valvular aortic stenosis. Magn Reson Med 2004;51:135-139
103. Biederman RW, Doyle M, Young AA, Devereux RB, Kortright E, Perry G, Bella JN, Oparil S, Calhoun D, Pohost GM, Dell'Italia LJ. Marked regional left ventricular heterogeneity in hypertensive left ventricular hypertrophy patients: a losartan intervention for endpoint reduction in hypertension (LIFE) cardiovascular magnetic resonance and echocardiographic substudy. Hypertension 2008;52:279-286
104. Kuijpers D, Ho KY, van Dijkman PR, Vliegenthart R, Oudkerk M. Dobutamine cardiovascular magnetic resonance for the detection of myocardial ischemia with the use of myocardial tagging. Circulation 2003;107:1592-1597
105. Bove CM, DiMaria JM, Voros S, Conaway MR, Kramer CM. Dobutamine response and myocardial infarct transmurality: functional improvement after coronary artery bypass grafting--initial experience. Radiology 2006;240:835-841
106. Gilson WD, Yang Z, French BA, Epstein FH. Measurement of myocardial mechanics in mice before and after infarction using multislice displacement-encoded MRI with 3D motion encoding. Am J Physiol Heart Circ Physiol 2005;288:H1491-1497
107. Fogel MA, Weinberg PM, Hubbard A, Haselgrove J. Diastolic biomechanics in normal infants utilizing MRI tissue tagging. Circulation 2000;102:218-224
108. Rosen BD, Gerber BL, Edvardsen T, Castillo E, Amado LC, Nasir K, Kraitchman DL, Osman NF, Bluemke DA, Lima JA. Late systolic onset of regional LV relaxation demonstrated in three-dimensional space by MRI tissue tagging. Am J Physiol Heart Circ Physiol 2004;287:H1740-1746
109. Rosen BD, Edvardsen T, Lai S, Castillo E, Pan L, Jerosch-Herold M, Sinha S, Kronmal R, Arnett D, Crouse JR, 3rd, Heckbert SR, Bluemke DA, Lima JA. Left ventricular concentric remodeling is associated with decreased global and regional systolic function: the Multi-Ethnic Study of Atherosclerosis. Circulation 2005;112:984-991
110. Arts T, Reneman RS, Veenstra PC. A model of the mechanics of the left ventricle. Ann Biomed Eng 1979;7:299-318

111. Rijcken J, Bovendeerd PH, Schoofs AJ, van Campen DH, Arts T. Optimization of cardiac fiber orientation for homogeneous fiber strain during ejection. Ann Biomed Eng 1999;27:289-297
112. Delhaas T, Kroon W, Bovendeerd P, Arts T. Left ventricular apical torsion and architecture are not inverted in situs inversus totalis. Prog Biophys Mol Biol 2008;97:513-519
113. Wang VY, Casta C, Croisille P, Clarysse P, Zhu YM, Cowan BR, Young AA, Nash MP. Estimation of in vivo human myocardial fibre strain by integrating diffusion tensor and tagged MRI using FE modelling. In, IEEE Symposium on Biomedical Imaging (ISBI). Barcelona: IEEE; 2012:46-49
114. Arts T, Meerbaum S, Reneman RS, Corday E. Torsion of the left ventricle during the ejection phase in the intact dog. Cardiovasc Res 1984;18:183-193
115. Lumens J, Delhaas T, Arts T, Cowan BR, Young AA. Impaired subendocardial contractile myofiber function in asymptomatic aged humans, as detected using MRI. Am J Physiol Heart Circ Physiol 2006;291:H1573-1579
116. Russel IK, Brouwer WP, Germans T, Knaapen P, Marcus JT, van der Velden J, Gotte MJ, van Rossum AC. Increased left ventricular torsion in hypertrophic cardiomyopathy mutation carriers with normal wall thickness. J Cardiovasc Magn Reson 2011;13:3
117. LeGrice IJ, Takayama Y, Covell JW. Transverse shear along myocardial cleavage planes provides a mechanism for normal systolic wall thickening. Circ Res 1995;77:182-193
118. Costa KD, Takayama Y, McCulloch AD, Covell JW. Laminar fiber architecture and three-dimensional systolic mechanics in canine ventricular myocardium. Am J Physiol 1999;276:H595-607
119. Cheng A, Nguyen TC, Malinowski M, Daughters GT, Miller DC, Ingels NB, Jr. Heterogeneity of left ventricular wall thickening mechanisms. Circulation 2008;118:713-721
120. Ubbink SW, Bovendeerd PH, Delhaas T, Arts T, van de Vosse FN. Towards model-based analysis of cardiac MR tagging data: relation between left ventricular shear strain and myofiber orientation. Med Image Anal 2006;10:632-641
121. Geerts L, Bovendeerd P, Nicolay K, Arts T. Characterization of the normal cardiac myofiber field in goat measured with MR-diffusion tensor imaging. Am J Physiol Heart Circ Physiol 2002;283:H139-145
122. Mazziotta J, Toga A, Evans A, Fox P, Lancaster J, Zilles K, Woods R, Paus T, Simpson G, Pike B, Holmes C, Collins L, Thompson P, MacDonald D, Iacoboni M, Schormann T, Amunts K, Palomero-Gallagher N, Geyer S, Parsons L, Narr K, Kabani N, Le Goualher G, Boomsma D, Cannon T, Kawashima R, Mazoyer B. A probabilistic atlas and reference system for the human brain: International Consortium for Brain Mapping (ICBM). Philos Trans R Soc Lond B Biol Sci 2001;356:1293-1322
123. Kohane IS. The twin questions of personalized medicine: who are you and whom do you most resemble? Genome Med 2009;1:4
124. Young AA, Frangi AF. Computational cardiac atlases: from patient to population and back. Exp Physiol 2009;94:578-596
125. Fonseca CG, Backhaus M, Bluemke DA, Britten RD, Chung JD, Cowan BR, Dinov ID, Finn JP, Hunter PJ, Kadish AH, Lee DC, Lima JA, Medrano-Gracia P, Shivkumar K, Suinesiaputra A, Tao W, Young AA. The Cardiac Atlas Project--an imaging database for computational modeling and statistical atlases of the heart. Bioinformatics 2011;27:2288-2295
126. Medrano-Gracia P, Backhaus M, Bluemcke D, Chung JD, Cowan BR, Finn JP, Fonseca CG, Hunter PJ, Kadish AH, Lee DC, Lima JAC, Shivkumar K, Tao W, Young AA. The cardiac atlas project: rationale, design and preliminary results. Journal of Cardiovascular Magnetic Resonance 2011;13:O72
127. Kadish AH, Bello D, Finn JP, Bonow RO, Schaechter A, Subacius H, Albert C, Daubert JP, Fonseca CG, Goldberger JJ. Rationale and design for the Defibrillators to Reduce Risk by

Magnetic Resonance Imaging Evaluation (DETERMINE) trial. J Cardiovasc Electrophysiol 2009;20:982-987
128. Ryan A, Eklund P, Esler B. Toward the interoperability of HL7 v3 and SNOMED CT: a case study modeling mobile clinical treatment. Stud Health Technol Inform 2007;129:626-630
129. Rosse C, Mejino JL, Jr. A reference ontology for biomedical informatics: the Foundational Model of Anatomy. J Biomed Inform 2003;36:478-500
130. Kundu S, Itkin M, Gervais DA, Krishnamurthy VN, Wallace MJ, Cardella JF, Rubin DL, Langlotz CP. The IR Radlex Project: an interventional radiology lexicon--a collaborative project of the Radiological Society of North America and the Society of Interventional Radiology. J Vasc Interv Radiol 2009;20:S275-277
131. Mega MS, Dinov ID, Mazziotta JC, Manese M, Thompson PM, Lindshield C, Moussai J, Tran N, Olsen K, Zoumalan CI, Woods RP, Toga AW. Automated brain tissue assessment in the elderly and demented population: construction and validation of a sub-volume probabilistic brain atlas. Neuroimage 2005;26:1009-1018
132. Tang Y, Hojatkashani C, Dinov ID, Sun B, Fan L, Lin X, Qi H, Hua X, Liu S, Toga AW. The construction of a Chinese MRI brain atlas: a morphometric comparison study between Chinese and Caucasian cohorts. Neuroimage 2010;51:33-41
133. Camara O, Konukoglu E, Pop M, Rhode K, Sermesant M, Young AA. Statistical Atlases and Computational Models of the Heart: Imaging and Modelling Challenges; 2011
134. Camara O, Pop M, Rhode K, Sermesant M, Young AA. Statistical Atlases and Computational Models of the Heart; 2010
135. Wang VY, Lam HI, Ennis DB, Cowan BR, Young AA, Nash MP. Modelling passive diastolic mechanics with quantitative MRI of cardiac structure and function. Med Image Anal 2009;13:773-784
136. Nash MP, Hunter PJ. Computational mechanics of the heart. J Elasticity 2000;61:113-141
137. Wang VY, Lam HI, Ennis DB, Cowan BR, Young AA, Nash MP. Cardiac active contraction parameters estimated from magnetic resonance imaging. In, Statistical Atlases and Computational Models of the Heart: LNCS; 2010:194-203
138. Shi P, Liu H. Stochastic finite element framework for simultaneous estimation of cardiac kinematic functions and material parameters. Med Image Anal 2003;7:445-464
139. Chabiniok R, Moireau P, Lesault PF, Rahmouni A, Deux JF, Chapelle D. Estimation of tissue contractility from cardiac cine-MRI using a biomechanical heart model. Biomech Model Mechanobiol 2011;11:609-630
140. Xi J, Lamata P, Lee J, Moireau P, Chapelle D, Smith N. Myocardial transversely isotropic material parameter estimation from in-silico measurements based on a reduced-order unscented Kalman filter. J Mech Behav Biomed Mater 2011;4:1090-1102
141. Sermesant M, Moireau P, Camara O, Sainte-Marie J, Andriantsimiavona R, Cimrman R, Hill DL, Chapelle D, Razavi R. Cardiac function estimation from MRI using a heart model and data assimilation: advances and difficulties. Med Image Anal 2006;10:642-656
142. Wang VY, Ennis DB, Young AA, Nash MP. Myocardial contractility and regional work throughout the cardiac cycle using FEM and MRI. In, Statistical Atlases and Computational Models of the Heart: LNCS; 2012:149-159
143. Lanir Y. Constitutive equations for fibrous connective tissues. J Biomech 1983;16:1-12
144. Criscione JC, McCulloch AD, Hunter WC. Constitutive framework optimized for myocardium and other high-strain, laminar materials with one fiber family. Journal of the Mechanics and Physics of Solids 2002;50:1681-1702

145. Wen H, Bennett E, Epstein N, Plehn J. Magnetic resonance imaging assessment of myocardial elastic modulus and viscosity using displacement imaging and phase-contrast velocity mapping. Magn Reson Med 2005;54:538-548
146. Young AA, Li B, Kirton RS, Cowan BR. Generalized spatiotemporal myocardial strain analysis for DENSE and SPAMM imaging. Magn Reson Med 2011
147. Lustig M, Donoho D, Pauly JM. Sparse MRI: The application of compressed sensing for rapid MR imaging. Magn Reson Med 2007;58:1182-1195